*J. Fluid Mech.* (1995), *vol.* 295, *pp.* 199–227



# Shear-free turbulent boundary layers. Part 1. Physical insights into near-wall turbulence

By BLAIR PEROT† AND PARVIZ MOIN‡
Department of Mechanical Engineering, Stanford University, Stanford, CA 94305 USA

(Received 10 January 1994 and in revised form 18 February 1995)

Direct numerical simulation is used to examine the interaction of turbulence with a wall in the absence of mean shear. The influence of a solid wall on turbulence is analysed by first considering two 'simpler' types of boundaries. The first boundary is an idealized permeable wall. This boundary isolates and elucidates the viscous effects created by the wall. The second boundary is an idealized free surface. This boundary complements the first by allowing one to isolate and investigate the kinematic effects that occur near boundaries. The knowledge gained from these two simpler flows is then used to understand how turbulence is influenced by solid walls where both viscous and kinematic effects occur in combination.

Examination of the instantaneous flow fields confirms the presence of previously hypothesized structures (splats), and reveals an additional class of structures (antisplats). Statistical analysis of the Reynolds stresses and Reynolds stress transport equations indicates the relative importance of dissipation, intercomponent energy transfer, and energy transport. It is found that it is not the structures themselves, but the imbalance between structures which leads to intercomponent energy transfer. Remarkably, this imbalance (and hence near-wall intercomponent energy transfer) is controlled by viscous processes such as dissipation and diffusion. The analysis presented herein is a departure from past notions of how boundaries influence turbulence. The efficacy of these qualitative physical concepts is demonstrated in Part 2 where improved near-wall turbulence models are derived based on these ideas.

## 1. Introduction

Walls affect turbulence through a number of different mechanisms. The most prominent and well-understood mechanism is that due to mean shear. But other more subtle mechanisms also exist and can be isolated through the study of shear-free boundary layers where the influence of mean shear has been eliminated.

Understanding the interaction of turbulence with a solid wall is of fundamental importance to basic turbulence research. Many situations which are particularly difficult to model (stagnation points, separation, reattachment) intimately involve the influence of a boundary on turbulence. Understanding how a solid wall interacts with turbulence is the key to improving the predictive capabilities of near-wall models, and is the motivation for this work.

A great deal is understood about how mean shear influences near-wall turbulence. Kline *et al.* (1967), and later Moin (1987) and Robinson (1991), showed that turbulence production is intimately associated with the streamwise vortices and streaky

† Currently at Los Alamos National Laboratory, NM 87545, USA.
‡ Also with NASA-Ames Research Center, Moffett Field, CA 94035, USA.

structures that are found in the near-wall region. It has also been demonstrated by Lee, Kim & Moin (1990) that streaky structures are a direct result of large mean shear.

However, many boundary layers have regions where mean shear is not the dominant mechanism; examples are high free-stream turbulent boundary layers, free-surface flows, and in many circumstances separating and reattaching flows. In these regions the wall (or surface) continues to have a very profound effect on the turbulence behaviour but the processes which are at work are not as well understood as in the shearing case. This is reflected by the fact that many turbulence models have difficulty in accurately predicting these flows. Shear-free turbulent boundary layers provide a means of isolating some of the more subtle interactions that occur between turbulence and a solid wall and should help to elucidate the physics that is currently missing from most near-wall turbulence models.

### 1.1. *Background*

The first experiments on shear-free boundary layers were performed by Uzkan & Reynolds in 1967. In these experiments a shear-free boundary layer was created by passing grid-generated water-tunnel turbulence over a belt that moved at the mean velocity of the fluid. In this arrangement the turbulence far from the belt decayed as it moved downstream. Closer to the wall, the turbulence decayed at a faster rate due to the presence of the wall. Uzkan & Reynolds measured the streamwise turbulent intensities at a number of stations along the belt. They quantified the turbulence 'damping' produced by the belt and showed that the damping region scaled on a viscous lengthscale.

In 1977, Thomas & Hancock performed a very similar moving belt experiment in air. Their measurements were more detailed and included all the turbulent intensities. Remarkably, they obtained substantially different results from their predecessors. The streamwise turbulent intensity increased as one approached the wall rather than being damped. In a primarily theoretical paper Hunt & Graham (1978) attempted to reconcile these differences. They suggested that the different behaviours were a result of a competition between two different mechanisms, one viscous and therefore dynamic, the other essentially kinematic. In the experiments of Uzkan & Reynolds the viscous effects dominated because the Reynolds number was relatively low ($Re_T = k^2/\nu\epsilon \approx 90$). On the other hand the experiments of Thomas & Hancock, at $Re_T \approx 2000$, allowed the kinematic effects (often referred to as wall blocking effects), to control the near-wall behaviour.

Biringen & Reynolds (1981) attempted to numerically simulate these shear-free turbulent boundary layers. They used large-eddy simulation, and so their results were limited by grid resolution and the subgrid-scale models available at the time. Their simulations did show, very generally, the right Reynolds number trends, but it is not clear whether this is a result of higher Reynolds numbers or a result of using a no-stress boundary condition (rather than no slip) for the higher Reynolds number simulation.

The present work uses direct numerical simulation to study several different types of shear-free boundaries at various Reynolds numbers. Detailed instantaneous and statistical measurements of the flow have been calculated, including terms in the Reynolds stress evolution equations. For an analysis of heat transfer in shear-free turbulent boundary layers see the related work of Malan & Johnston (1993). Experimental studies involving mild mean shear, and heat transfer, are currently underway by Bradshaw & Bott (1993). Simulations of boundary layers with mild shear, and additional statistical results from this work can be found in Perot & Moin (1993).

### 1.2. *Review of near-wall physics*

The experiments of Uzkan & Reynolds and Thomas & Hancock revealed that the effects of a solid wall on turbulence, even in the absence of mean shear, are quite complicated. Viscous effects damp the turbulence intensities, while wall blocking effects can amplify tangential turbulent intensities. An event (or structure) called a 'splat' is used to explain how tangential turbulent intensities can increase near a wall (such as was the case in the Thomas & Hancock experiments). A splat is a local region of stagnation point flow resulting from fluid impinging on the boundary. Because fluid cannot penetrate the boundary (wall blocking), any fluid moving towards a wall must eventually turn and move parallel to the wall. In this way, a splat event transfers energy from the normal velocity component to the two tangential velocity components, increasing the tangential turbulence intensity near the wall.

In homogeneous flows, energy transfer of this type (between various velocity components) is typically associated with the pressure–strain term of the Reynolds stress transport equations. In inhomogeneous flows, other terms (such as the dissipation) could also potentially contribute to the redistribution of energy among the various velocity components. However, the pressure–strain term is still considered to be principally responsible for intercomponent energy transfer in these shear-free flows. This is because splat events (responsible for intercomponent energy transfer) have a region of high pressure and strongly decelerating flow associated with them, and these are exactly the elements required to exhibit a strong pressure-strain correlation.

The intercomponent energy transfer mechanisms that occur near boundaries are fundamentally different from those that occur in homogeneous turbulence. This is reflected very clearly in the pressure–strain term. In homogeneous turbulence, the pressure–strain term tends to isotropize turbulence. Near walls (even shearing walls) pressure–strain tends to move turbulence away from isotropy. A deeper understanding of shear-free boundary layers, and in particular splats, could be the key to better pressure–strain modelling, and improved near-wall turbulence models.

It is the goal of this paper to analyse, in detail, the hypotheses and assumptions embedded in the paragraphs above. These hypothesis are often the basis for turbulence models (see Durbin 1993 and Brumley 1984 for examples). We will find that although the previous analyses are very useful, they require considerable alterations and adjustments to explain the results of our simulations.

### 1.3. *Overview*

The numerical details and the computational configuration used to simulate the different shear-free boundary layers are presented in §2. Results from simulations of turbulence near a perfectly permeable wall are presented and discussed in §3. The complementary boundary, an ideal free surface, is analysed in §4. As opposed to the permeable wall, this flow is dominated by wall blocking and has only mild viscous effects. Only when these simpler boundaries are fully understood do we propose to analyse how a standard solid wall influences turbulence (§5). Finally, §6 presents a short discussion and a summary of the major conclusion of this work. Appendix A contains an overview of the inviscid rapid distortion theory (RDT) (Hunt & Graham) analysis and a discussion of its range of applicability, and Appendix B discusses the viscous near-wall Hunt & Graham analysis. Part 2 of this series (Perot & Moin 1995) goes on to extend the qualitative ideas developed in this paper to quantitative improvements in near-wall turbulence modelling.

## 2. Simulation details

### 2.1. *Numerical discretization*

The results presented in this study are based on direct numerical simulations of the unsteady incompressible constant-property Navier–Stokes equations,

$$\nabla \cdot \boldsymbol{u} = 0, \tag{2.1a}$$

$$\frac{\partial \boldsymbol{u}}{\partial t} + (\boldsymbol{u} \cdot \nabla)\boldsymbol{u} = -\nabla p + \frac{1}{Re}\nabla^2 \boldsymbol{u}. \tag{2.1b}$$

All essential scales of motion are computationally resolved; no modelling of the small-scale turbulence is needed.

A second-order, finite-volume method, on a Cartesian staggered mesh is used to discretize the equations of motion. The discretization is very much in the spirit of Harlow & Welch (1965) and Kim & Moin (1985). Lilly (1965) showed that in the absence of viscosity, this scheme conserves energy, momentum, and vorticity. Details of the discretization are given in Le (1994). The performance of the method, on the Connection Machine and the Cray Y-MP is discussed in Perot (1992).

The computational box size of the simulations is large enough so that the flow variables are not correlated across the computational box. This was ensured by examining two-point velocity correlations. In agreement with other direct numerical simulations, a box size equal to about five times the wavelength of the peak energy-containing wavenumber was found to be sufficient. The grid resolution, on the other hand, is a function of the Reynolds number. In the simulations that we will be discussing various grid sizes were used, depending on the Reynolds number. In all cases, the grid resolution used in these simulations is in close agreement with other well-resolved simulations and the predictions of Reynolds (1991).

The nonlinear convective terms are advanced in time with a third-order Runge–Kutta method. The stability limit imposed by the explicit Runga–Kutta method is not overly restrictive and corresponds roughly to the condition that the temporal accuracy matches the spatial accuracy (in a Taylor's hypothesis sense). The diffusive terms are advanced implicitly with the trapezoidal (Crank–Nicolson) method, to avoid stability restrictions. Finally, the pressure is updated using the fractional step method. This time advancement scheme differs from that of Kim & Moin (1985) in only a few ways. First, the diffusive terms are updated only once, not at every substep of the Runge–Kutta advancement. This allows the Runge–Kutta scheme to be simpler and have a CFL stability limit of 2 rather than $\sqrt{3}$. This type of operator splitting was studied by Maday, Patera & Ronquist (1990), and was shown to be mathematically and computationally sound. Secondly, an improved fractional step method was implemented which overcomes previously problematic boundary condition and time accuracy issues. This improvement is accomplished by performing the spatial discretization before the operator splitting, rather than after (Perot 1993).

### 2.2. *Configuration*

It was mentioned in the papers of both Uzkan & Reynolds and Thomas & Hancock that the ideal shear-free turbulent boundary layer is created by instantaneously inserting an infinite flat plate into homogeneous isotropic turbulence. This creates a boundary layer where statistical properties depend only on time and the distance from the wall. This temporally growing shear-free boundary layer is statistically homogeneous in planes parallel to the wall. The mechanical difficulties associated with

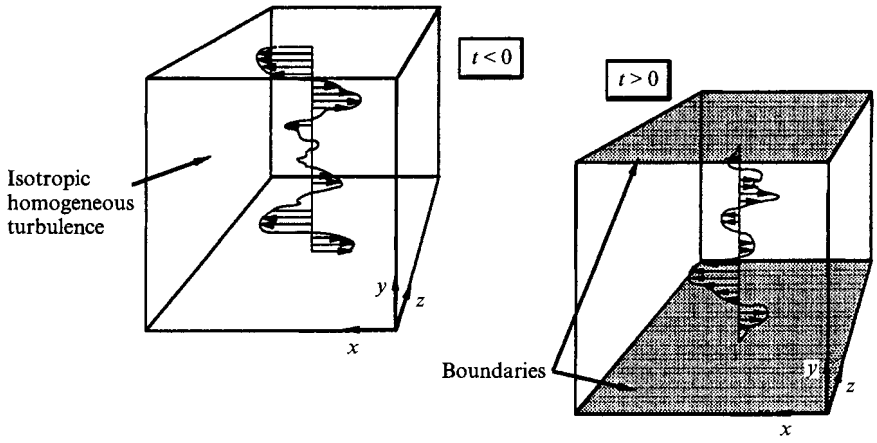


FIGURE 1. Schematic representation of computational configuration used to simulate temporally growing shear-free turbulent boundary layers.

instantaneously inserting a flat plate into turbulence led to the use of the moving belt configuration for the experimental studies of Uzkan & Reynolds and Thomas & Hancock. The current configuration (temporally developing) is related to the experimental studies (spatially developing) via Taylor's hypothesis. The temporally growing layer is somewhat 'cleaner' since there are no streamwise derivatives. These streamwise derivatives are particularly influential at the leading edge of the spatially growing layer, and their effects can be felt for long distances downstream because (unlike standard boundary layers) there is no production or mean flow present which can quickly reorganize the turbulence.

An example of the configuration is shown in figure 1. The simulation starts with a large (periodic) box of turbulence. Then at a particular time (arbitrarily labelled $t = 0$), boundaries are instantaneously introduced at the top and bottom faces of the computational domain. As time progresses, boundary layers grow away from the boundaries. These boundary layers consist of large variations in the statistical properties of the fluid. They do not have a mean flow associated with them, since the mean flow is zero everywhere in these simulations. The simulation ends just before the top and bottom layers are close enough to begin interacting with each other. Boundaries are placed at both the top and bottom faces of the domain in order to double the available statistical sample. Periodic boundary conditions are used for the other faces of the domain, and grid refinement is used near the boundaries in order to adequately capture the developing layers there.

### 2.3. *Boundary insertion*

The instantaneous appearance of a boundary in a turbulent fluid is a process that requires some attention, particularly when the boundary is impenetrable ($v = 0$ on the boundary). Sudden imposition of the $v = 0$ boundary condition on an initially incompressible velocity field would, in the absence of pressure, cause continuity to be violated at the boundary. The pressure preserves continuity by responding to the $v = 0$ boundary condition, and instantaneously redistributing energy among the velocity components appropriately.

Mathematically, this process is equivalent to projecting the dilatational velocity field (created by the instantaneous imposition of $v = 0$) into the space of incompressible velocity fields. Numerically, this projection can be easily accomplished by drastically

reducing the time step of the simulation when the boundary is inserted. In both cases, the result is the Hunt & Graham solution for high Reynolds number wall-bounded flows.

The Hunt & Graham RDT analysis is exact for the case of boundary insertion (see Appendix A). The analysis predicts that the sudden presence of wall blocking ($v = 0$) will reduce the normal component of the turbulence intensity over roughly one large-eddy length away from the boundary, and cause a corresponding amplification in the tangential turbulence intensities. This energy redistribution occurs instantaneously in order to preserve continuity when the boundary is inserted. This implies that for the free surface and solid wall boundaries, the turbulence is not homogeneous immediately after boundary insertion (at $t = 0^+$). The subsequent evolution of the turbulence will be influenced by both the boundary and the initial inhomogeneity in the turbulence. This makes the results of these simulations somewhat harder to interpret, but does not fundamentally change any of the conclusions that are drawn from the results.

### 2.4. *Parameters and statistics*

The relevant Reynolds number for these shear-free flows is the turbulent Reynolds number, $Re_T = k^2/\epsilon\nu$, where $k$ is the turbulent kinetic energy, $\epsilon$ is the turbulent dissipation rate, and $\nu$ is the kinematic viscosity. This is a result of using $k^{1/2}$ as the relevant velocity scale, and the large-eddy length, $L = k^{3/2}/\epsilon$, as the relevant lengthscale. For homogeneous isotropic turbulence, the turbulent Reynolds number is related to the more commonly quoted longitudinal Taylor microscale Reynolds number by $Re_T = \frac{3}{20}Re_\lambda^2$. Here $Re_\lambda = u'\lambda/\nu$ where $u' = (\overline{u'^2})^{1/2}$ and $\lambda$ is the longitudinal Taylor microscale (Batchelor 1956). As a basis for comparison in what follows, the experiments of Uzkan & Reynolds had a turbulent Reynolds number of approximately 90, and that of Thomas & Hancock was about 2000.

Statistics of the turbulence were evaluated by averaging over the homogeneous $x$- and $z$-directions, and additionally through the use of ensemble averaging. Each realization in the ensemble is produced by running the simulation under the same flow parameters but with a different initial condition. The statistics far from the boundary, in the far-field region, typically take the longest time to converge since lengthscales are largest there. Owing to restrictions on computational resources, and the large number of simulations (realizations) required for this study, some of the statistical results show oscillations in the far field due to the lack of statistical sample. We judged it a poor use of computational resources to smooth these oscillations further. The number of realizations that are required in each case is a function of the grid resolution, the Reynolds number of the turbulence, and the boundary being studied.

In addition to determining the Reynolds stresses, all the terms in the Reynolds stress evolution equations,

$$R_{ij,t} = -(Q_{i,j} + Q_{j,i}) + \frac{1}{Re} R_{ij,kk} - T_{ijk,k} - \epsilon_{ij} + \Pi_{ij} \tag{2.2}$$

were evaluated. $R_{ij} = \overline{u_i u_j}$ is the Reynolds stress tensor, $Q_i = \overline{pu_i}$ is the pressure–velocity correlation, $T_{ijk} = \overline{u_i u_j u_k}$ is the triple correlation tensor, $\epsilon_{ij} = (2/Re)\overline{u_{i,k} u_{j,k}}$ is the homogeneous dissipation rate tensor, and finally $\Pi_{ij} = \overline{p(u_{i,j} + u_{j,i})}$ is the pressure–strain term. When the mean velocity is zero (as is the case in this work), then the pressure–strain term is equal to the slow pressure–strain (Rotta 1951). Since the production term, $P_{ij} = -(U_{i,k} R_{jk} + U_{j,k} R_{ik})$ and the convective term $U_k R_{ij,k}$ are identically zero for the flows under consideration, they do not appear in (2.2).

Results will only be presented for the tangential $R_{11}$ and normal $R_{22}$ components of

the Reynolds stress tensor. Since these flows are statistically axisymmetric, $R_{33} = R_{11}$ and all off-diagonal stresses are zero.

### 2.5. *Boundaries*

The perfectly permeable wall studied herein allows flow to move unimpeded through the boundary, but prohibits any motion tangential to the wall. Although unusual, the permeable wall has some very interesting physical properties. Most importantly, it does not result in wall blocking. This allows the study of near-wall viscous effects to occur in isolation from the complicating influences of wall blocking. The numerical boundary conditions for the perfectly permeable wall are zero tangential velocity ($u = w = 0$), and a periodic normal velocity (i.e. no direct condition on the normal velocity). However, $\partial v/\partial y = 0$ is implicitly satisfied at the boundary because of the continuity equation.

Simulations were performed for turbulent Reynolds numbers, $Re_T$, of 6.2, 54, and 137. The two lower Reynolds number simulations used a grid size of $64 \times 128 \times 64$, though the lowest Reynolds number case probably does not require such a fine grid. The higher Reynolds number case required a $128 \times 256 \times 128$ grid. For converged statistics, 204 realizations were taken for the lowest Reynolds number case, and 102 realizations for the moderate Reynolds number case. Only four realizations were possible for the highest Reynolds number case, which means that the statistics are only marginally converged. Only one result from the higher Reynolds number case is reported. The two lower Reynolds number cases require roughly the same number of realizations to obtain the same degree of statistical convergence. The use of twice the number of realizations for the lowest Reynolds number case was done to get a rough idea of the effort required to obtain further smoothing of the statistical results.

The free surface studied in this work is 'ideal' in that it does not support surface waves. This corresponds physically to a very large surface tension. The behaviour of turbulence near a free surface has important practical implications for problems involving heat and mass transfer. Such problems are frequently of interest in chemical and environmental engineering where surface processes are often critically important. The ideal free surface may also be a useful approximation to high Reynolds number wall-bounded flows.

In many respects, the physics of the free surface is complementary to that of the perfectly permeable wall. It is dominated by wall blocking ($v = 0$), and presumably the splat effect, but has almost no viscous effects since there is no fluid stress at the surface. The free-surface boundary allows an in-depth analysis of the (essentially kinematic) blocking effects of a wall, without the complicating influence of viscous damping. Since much has been hypothesized about splats and their influence on near-wall behaviour, this boundary provides an ideal situation in which to test those hypotheses.

Turbulence near a free surface was simulated at two different Reynolds numbers. The first case has an initial Reynolds number of 54. It required a $64 \times 128 \times 64$ grid and 60 realizations. The second case has an initial turbulent Reynolds number of 134, and required a $128 \times 256 \times 128$ grid, and 54 realizations for converged statistics.

The solid wall boundary incorporates the blocking condition ($v = 0$) of the free surface, and the no-slip condition ($u = w = 0$) of the perfectly permeable wall. Accompanying the no-slip condition is the kinematic boundary condition mentioned above, $\partial v/\partial y = 0$. Not surprisingly, certain aspects of the solid wall strongly resemble either the perfectly permeable membrane or the free surface.

The solid wall simulations were performed at turbulent Reynolds numbers of 54, 134, and 374. The grid was doubled in each direction at each successive Reynolds

number (recall that the required number of grid points in DNS is $N^3 \approx 30 Re_T^{9/4}$). The largest Reynolds number case was simulated using a $256 \times 512 \times 256$ grid. In order to obtain converged statistics, 30 realizations were used at the lowest Reynolds number, and 54 realizations and two realizations respectively were used at the higher Reynolds numbers. The CPU time required by the highest Reynolds number simulation limits the number of realizations which may be obtained in a reasonable amount of time.

Note that the highest Reynolds number case ($Re_T = 374$, $Re_\lambda = 50$) does not bring us up to the high Reynolds number experiments of Thomas & Hancock ($Re_T = 2000$, $Re_\lambda = 120$). However these simulations are among the highest Reynolds numbers obtained to date using direct numerical simulation, and the range of Reynolds numbers simulated does allow one to (cautiously) extrapolate to higher Reynolds numbers.

## 3. Perfectly permeable wall

In the perfectly permeable wall simulations, it is found that the tangential Reynolds stress, $R_{11}$, rapidly collapses to a single profile when the tangential stress is normalized by its free-stream value $R_{11\infty}$ and the distance from the wall is normalized by the viscous scale, $(\nu t)^{1/2}$. This collapse happens in less than an eddy turnover time, $T_0$. Profiles of the tangential Reynolds stress are shown in figure 2 for various Reynolds numbers.

In addition to the measured profiles we have also plotted a theoretical profile for the tangential Reynolds stress in the limit as the Reynolds number goes to zero. This analytical solution is obtained by assuming that dissipation and diffusion dominate at low Reynolds numbers, and that Rotta's (1951) low Reynolds number dissipation model is exact in that limit. Alternatively, this solution can be obtained by solving a diffusion equation for the fluctuating velocity as was done by Hunt & Graham (see Appendix B).

The fact that the tangential stress rapidly collapses on a viscous scaling confirms that this flow is dominated by viscous effects. Note that, as the Reynolds number increases, the tangential Reynolds stress profiles become fuller, with steeper gradients near the boundary and a deeper penetration into the flow in terms of viscous units. (In dimensional units the penetration into the flow actually decreases with increasing Reynolds number.) The simulated profiles have the required $O(y^2)$ behaviour very close to the boundary.

It is clear that the low Reynolds number analytical solution ($Re_T = 0$) rapidly becomes a poor approximation, even at relatively low Reynolds numbers. This is primarily because this linear solution neglects the transport of turbulence by itself. This is made clear in figure 3, where terms in the budget of the tangential Reynolds stress are shown at two different Reynolds numbers. The terms are non-dimensionalized by the initial dissipation rate, $\epsilon_0$. The profiles are plotted at time $t/T_0 = 3.0$. As expected, dissipation and diffusion dominate the balance near the wall. However, even at these low Reynolds numbers, turbulent transport is also an important factor in the near-wall balance. The relative importance of turbulent transport also appears to increase significantly as the Reynolds number is increased. It is this term which is responsible for the change in shape of the tangential Reynolds stress with increasing Reynolds number.

The turbulent transport term is shown in figure 4. Three different times and two different Reynolds numbers are shown. Like the tangential Reynolds stress, the turbulent transport term collapses very rapidly when scaled on the viscous lengthscale. The strong Reynolds number dependence of this term is also very apparent. The fact

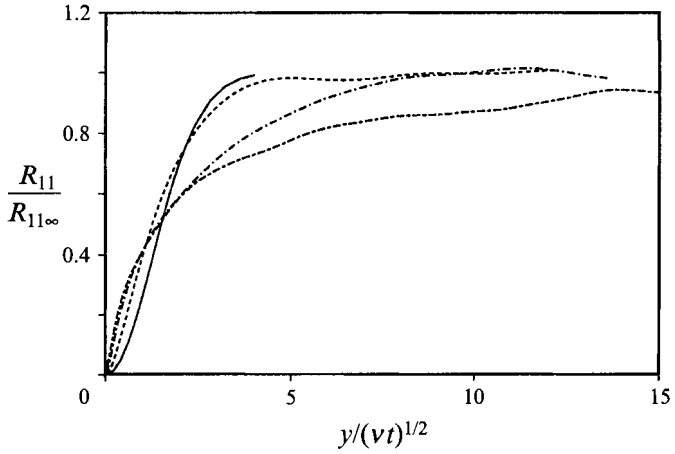


FIGURE 2. Reynolds number dependence of the tangential Reynolds stress ($t/T_0 = 3.1$): ——, $Re_T = 0$; – – –, $Re_T = 6.2$; — · —, $Re_T = 54$; — — —, $Re_T = 137$.

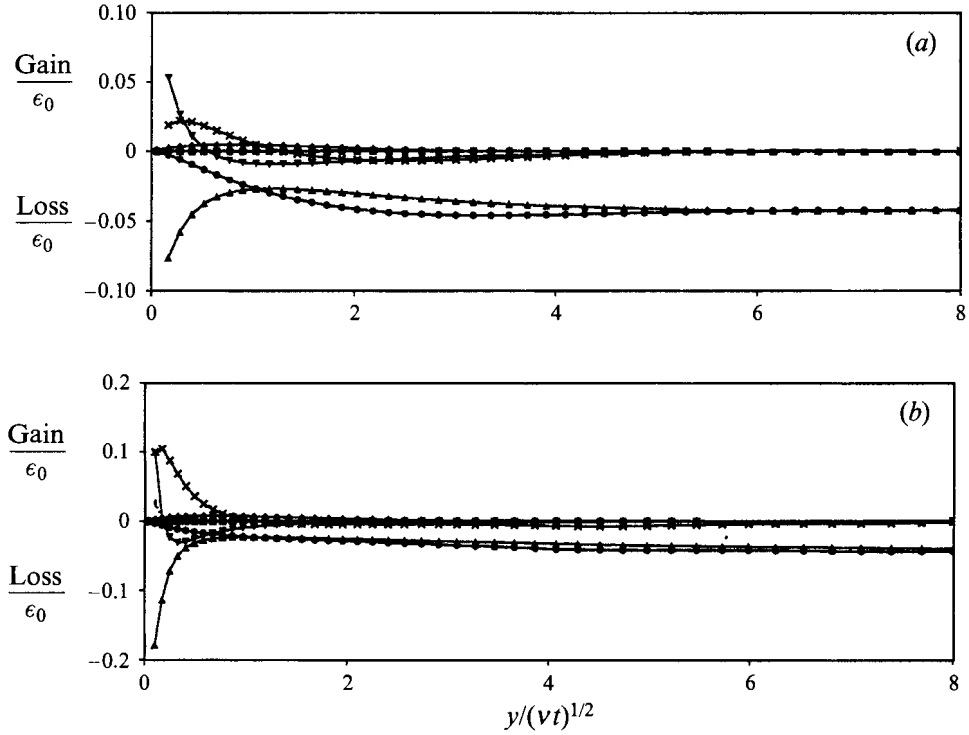


FIGURE 3. Terms in the budget of the tangential Reynolds stress for turbulence near a perfectly permeable wall ($t/T_0 = 3.0$). (*a*) $Re_T = 6.2$, (*b*) $Re_T = 54$; (●), time derivative; (◆), pressure–strain; (■), pressure transport; (×), turbulent transport; (▼), viscous diffusion; (▲), dissipation; ···|···, sum of all terms.

that the turbulent transport term and the tangential Reynolds stress both collapse on the same lengthscale parameter strongly suggests that the turbulent transport term can be modelled in terms of the tangential Reynolds stress. Since the turbulent transport term tends to make the tangential stress profiles fuller (increased effective viscosity), a gradient transport model would seem very appropriate in this context.

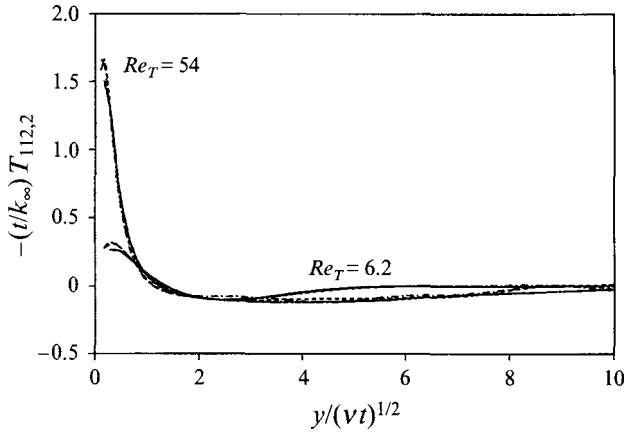


FIGURE 4. Collapse of the turbulent transport term for $Re_T = 6.2$ and 54: ——, $t/T_0 = 1.1$; – – – –, $t/T_0 = 2.1$; — · —, $t/T_0 = 3.1$.

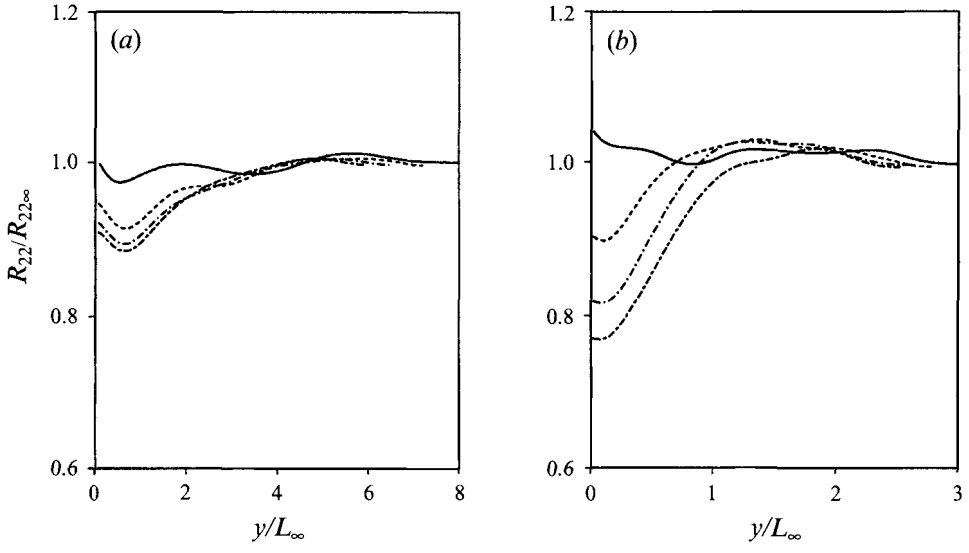


FIGURE 5. Scaled normal Reynolds stress profiles near a perfectly permeable wall. (*a*) $Re_T = 6.2$, (*b*) $Re_T = 54$: ——, $t/T_0 = 0.1$; – – – –, $t/T_0 = 1.1$; — · —, $t/T_0 = 2.1$; — – —, $t/T_0 = 3.1$.

The remaining term in the Reynolds stress equation balance is the pressure–strain term (pressure transport is identically zero for the tangential stresses), which is responsible for the transfer of energy between Reynolds stress components. It is relatively small, but not negligible. It can be significant at early times (when viscous effects are confined very close to the wall) and can contribute in the region far from the wall ($y/(\nu t)^{1/2} \approx 2$) where viscous effects are again relatively minor. We will also find that the pressure–strain term is crucial to explaining the behaviour of the normal stress component.

The normal Reynolds stress, $R_{22}$, near a permeable wall is shown in figure 5. Two different Reynolds numbers and several different times are shown. Unlike the tangential stress, the normal Reynolds stress does not collapse to a single profile when scaled in an appropriate way. However, normalizing the distance from the wall by the

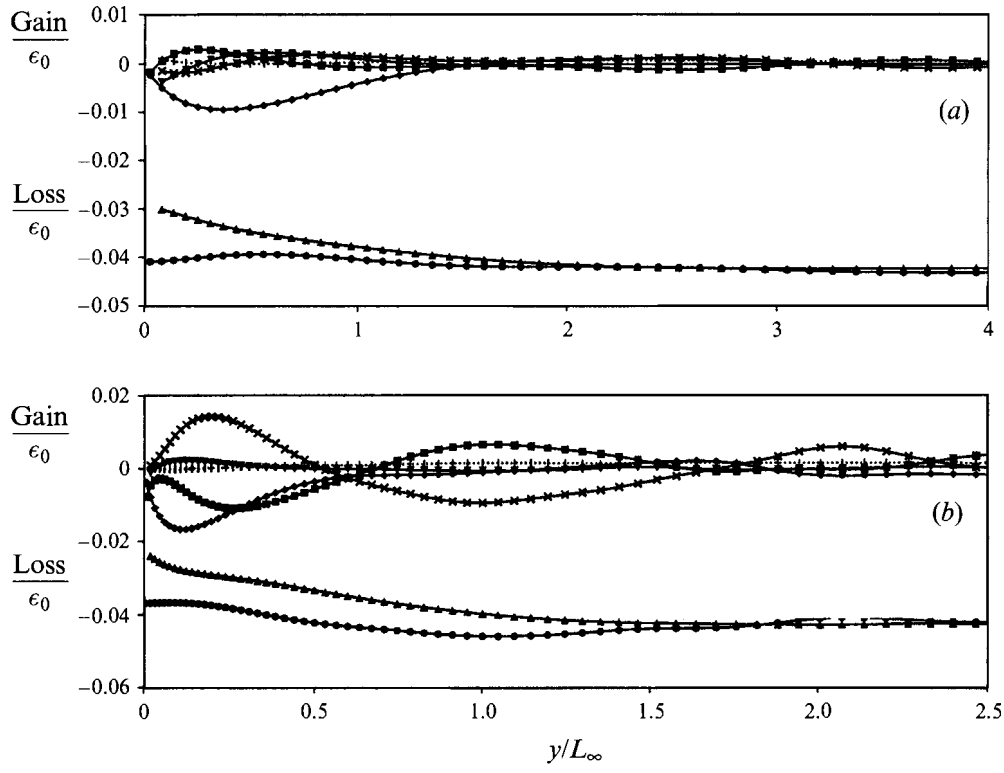


FIGURE 6. Terms in the normal Reynolds stress budget for turbulence near a perfectly permeable wall ($t/T_0 = 3.0$). (*a*) $Re_T = 6.2$, (*b*) $Re_T = 54$. See figure 3 for legend.

large-eddy lengthscale far from the wall, $L_\infty = (k^{3/2}/\epsilon)_\infty$, does appear to scale the extent of the 'inhomogeneity layer' near the wall. Note that $L_\infty$ grows with time as the turbulence decays.

Since there is no wall blocking ($v = 0$) in this flow, the inhomogeneity layer must be an indirect result of the boundary conditions on the tangential velocity. In fact, using the continuity equation it can be shown that the tangential velocity boundary conditions imply that $\partial v/\partial y = 0$ at the boundary. Figure 5 shows that the magnitude of the inhomogeneity layer increases with Reynolds number, while its extent ($y/L_\infty$) decreases. The Reynolds number behaviour of the inhomogeneity layer indicates that although the layer is closely associated with kinematic effects (via the continuity constraint) it also appears to have a strong viscous component to its behaviour.

Figure 6 helps to illuminate the underlying mechanisms of the inhomogeneity layer by showing the terms in the normal Reynolds stress budget at two different Reynolds numbers. The profiles are shown at time $t/T_0 = 3.0$ well after the layer has developed. The turbulent transport and pressure transport terms for the higher Reynolds number case may not be statistically converged far from the wall. The transport terms involve derivatives of statistics, and so they amplify small variations in the measured statistics.

The pressure–strain term makes a significant contribution to the normal stress evolution equation. Note that the pressure–strain is a sink term for the normal stress equation and a source term for the tangential stress equation, reflecting the fact that this term transfers energy from the normal to the tangential stress components. Also note that the scale on figure 6 is an order of magnitude smaller than that of the corresponding tangential stress budget (figure 3).

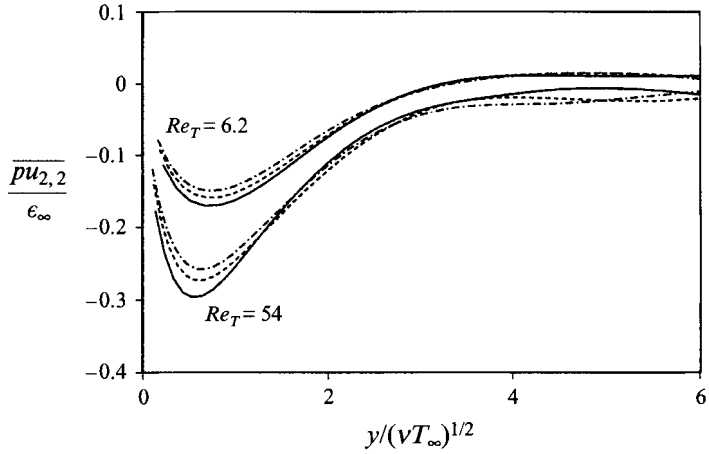


FIGURE 7. Collapse of the pressure–strain term for $Re_T = 6.2$ and $Re_T = 54$. ——, $t/T_0 = 1.1$; – – – –, $t/T_0 = 2.1$; — · —, $t/T_0 = 3.1$.

The magnitudes of the transport terms (pressure transport and turbulent transport) increase significantly as the Reynolds number increases. This is probably due to the larger gradients that are present in the inhomogeneity layer at higher Reynolds numbers. Note that the turbulent transport term near the boundary has a different sign for the two different Reynolds number cases. This is not a function of the Reynolds number, but of the viscous timescale (which is different for the two instances presented). The viscous terms (dissipation and diffusion) do not play a major role in the behaviour of the normal stress. The dissipation, although large, does not change significantly from its free-stream value as the wall is approached. It is also interesting that (at these long times) the time derivative changes very little across the domain. This indicates that the inhomogeneity layer has approached some sort of equilibrium state.

The equilibrium state can be described as follows. Energy is transferred from the normal stress to the tangential stresses by the pressure–strain term. This loss of energy in the near-wall region is replenished by the transport of energy from further out by the pressure transport and turbulent transport terms. The energy that is transferred to the tangential stress is quickly removed by the strong viscous effects associated with the tangential component.

Although the normal stress does not collapse on a convenient scaling, the pressure–strain term does. This is shown in figure 7 for two Reynolds numbers and several different times. The relative magnitude of the pressure–strain increases with increasing Reynolds number, and the extent of the pressure–strain scales on the length $(\nu T_\infty)^{1/2}$. The Reynolds number dependence of the pressure–strain has been hypothesized by Lumley (1978) and observed in simulations of anisotropic homogeneous turbulence (Hallback & Johansson 1992). The emergence of the lengthscale $(\nu T_\infty)^{1/2} = L_\infty / Re_T^{1/2}$ is much more surprising. This scaling suggests that the pressure–strain term, and hence energy transfer, is not solely a kinematic effect, but has strong ties to viscosity. How the energy transfer mechanisms present in this flow (with $\partial v/\partial y = 0$) compare with those due to wall blocking (with $v = 0$) is one of the subjects to be addressed in the next section.

## 4. Ideal free surface

The purpose of studying turbulence in the presence of an ideal free surface is to highlight the effects of wall blocking and the role of splat events. Figure 8 shows instantaneous snapshots of the flow which confirm the presence of the splat event and help to detail its structure. Figure 8(*a*) shows velocity vectors in a plane close to and parallel to the free surface. In addition to the velocity vectors, the shading on the figure shows the normal velocity. The turbulent Reynolds number is 54, and the time is $t/T_0 = 0.3$.

The splat regions (local stagnation points) are easy to identify: they are lightly shaded and the velocity vectors are small and point radially outwards. A typical splat is indicated on figure 8(*a*); they tend to be roughly axisymmetric. In addition to the splats, there are regions of ejecting fluid. These darker regions tend to form long fronts where two splats meet, and are sometimes associated with rotating fluid. These ejecting events will be referred to as *antisplats*. A typical antisplat is also indicated in figure 8(*a*). Although antisplats are an intuitive counterpart of splat events, they have not been discussed previously. We emphasize their presence here, because they are critical to explaining the near-wall behaviour of the free surface, and the solid wall simulations that follow.

Figure 8(*b*) is similar to figure 8(*a*) except that the shading shows the pressure, rather than normal velocity. The stagnation-point behaviour of the splats should be associated with higher pressure. This is indeed the case, but other high-pressure regions also exist, and are the result of the collision of two tangentially moving fluid bodies. Note that low pressure tends to be associated with the cores of rotating fluid regions. The pressure is, therefore, not a particularly good indicator of the presence of splats or antisplats.

The tangential Reynolds stress profiles for turbulence near an ideal free surface are shown in figure 9. The distance from the surface is normalized by the viscous lengthscale and the Reynolds stress is normalized by its far-field (isotropic) value. The lower Reynolds number case is shown in figure 9(*a*) at three different times, and the higher Reynolds number case is shown in figure 9(*b*) at four different times.

Recall that owing to boundary insertion (§2.3) the initial tangential stress (at $t^+ = 0$) is not homogeneous. The initial tangential stress profile increases as the boundary is approached. This type of behaviour continues even at later times. In fact, the magnitude of the tangential stress inhomogeneity actually increases slowly with time. Identical behaviour was observed in the high Reynolds number experiments of Thomas & Hancock (for the streamwise stress component).

Note that the peak in the tangential Reynolds stress near the wall does not grow indefinitely. Eventually an equilibrium profile is approached where the mechanism responsible for the peak is balanced by the increased diffusion and turbulent transport. This equilibrium profile is approached more rapidly at lower Reynolds numbers.

The Reynolds stress budgets for the tangential stress are shown in figure 10. Two Reynolds numbers are shown at time $t/T_0 = 3.0$. Remarkably, the pressure–strain term is small. Dissipation, diffusion, and turbulent transport are the dominant terms. This does not agree with the notion that a free surface is dominated by the presence of splat structures and energy transfer (via wall blocking).

The clear presence of splats (figure 8) and the lack of pressure–strain (energy transfer between stress components) can be reconciled by including antisplats into one's concept of the near-wall physics. Splats do indeed exist and transfer energy from the normal component of the velocity to the tangential component. However, antisplats

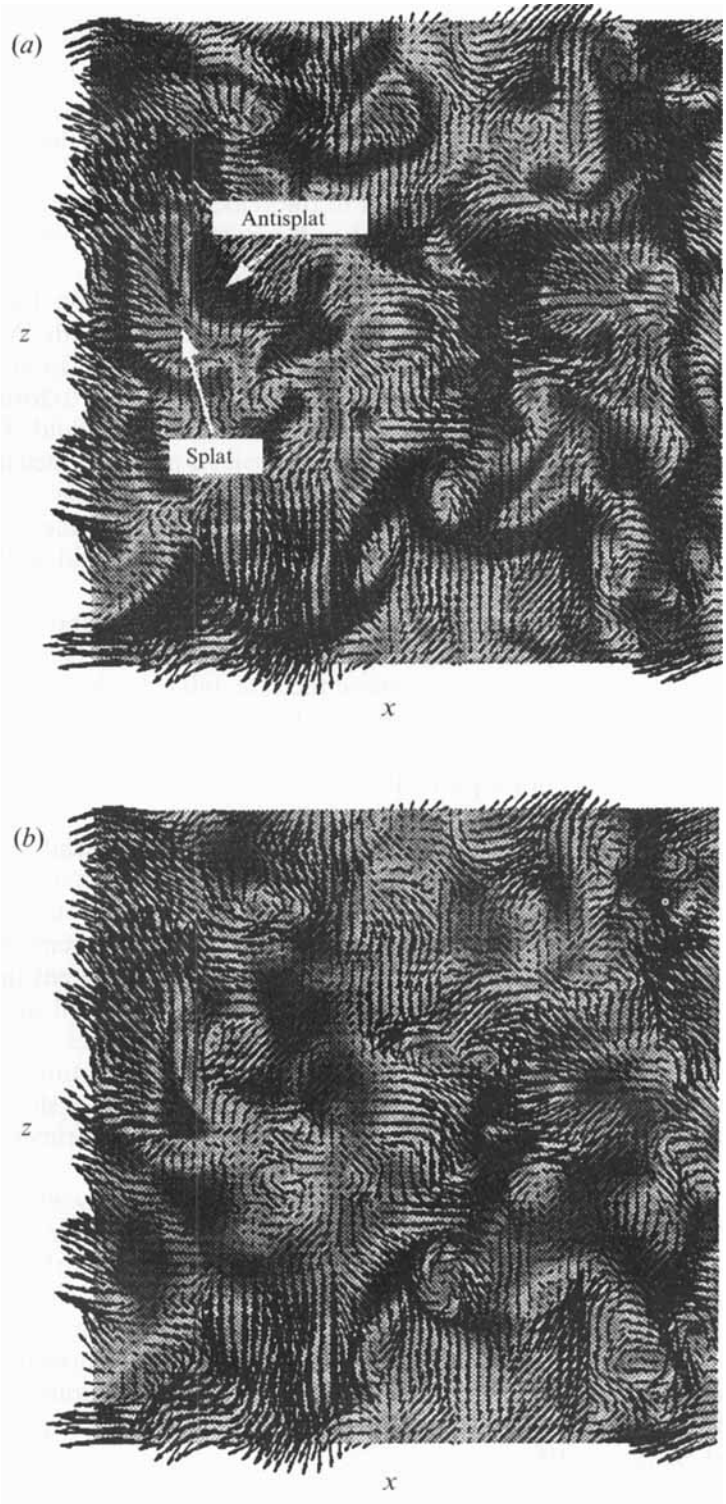


FIGURE 8. Velocity vectors in a plane parallel to the ideal free surface ($Re_\tau = 134$): (*a*) shading shows for normal velocity, lighter regions are impinging flow; (*b*) shaded pressure, lighter regions are low pressure.

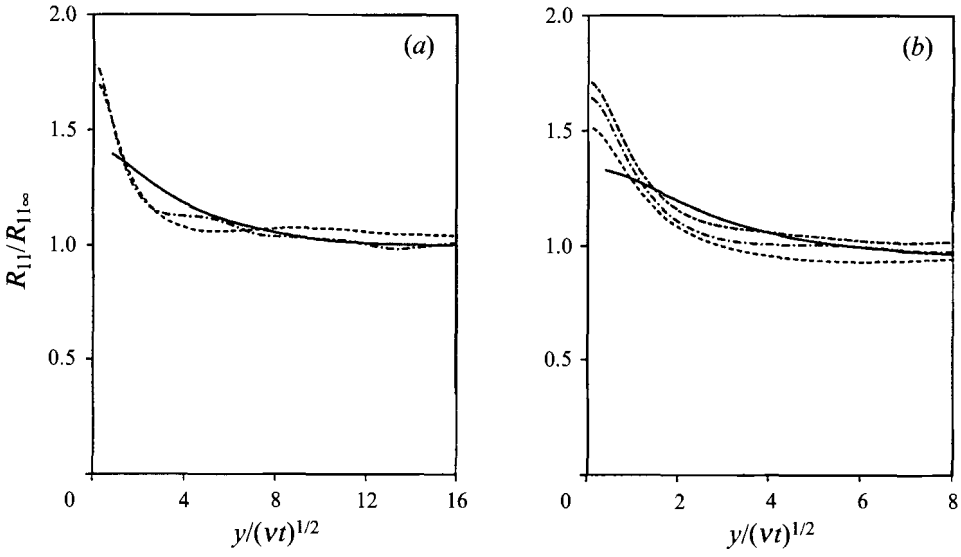


FIGURE 9. Tangential Reynolds stress profiles near an ideal free surface. (*a*) $Re_T = 54$, (*b*) $Re_T = 134$: ——, $t/T_0 = 0.1$; – – –, $t/T_0 = 1.1$; — · —, $t/T_0 = 2.1$; — — —, $t/T_0 = 3.1$.

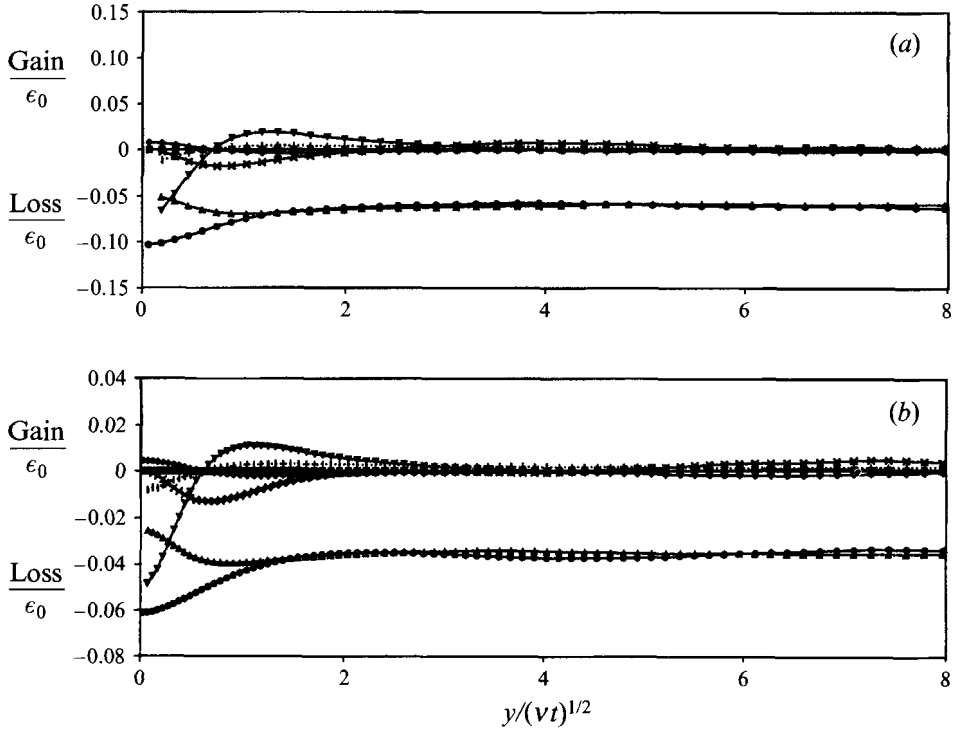


FIGURE 10. Terms in the tangential Reynolds stress budget for turbulence near an ideal free surface ($t/T_0 = 3.0$). (*a*) $Re_T = 54$, (*b*) $Re_T = 134$. See figure 3 for legend.

quickly transform that tangential velocity back into a normal velocity, so the net result is very little energy transfer, and hence a small pressure–strain term. This is an important point, which we will return to often. Neither splats nor antisplats are individually responsible for intercomponent energy transfer in the near-wall region.

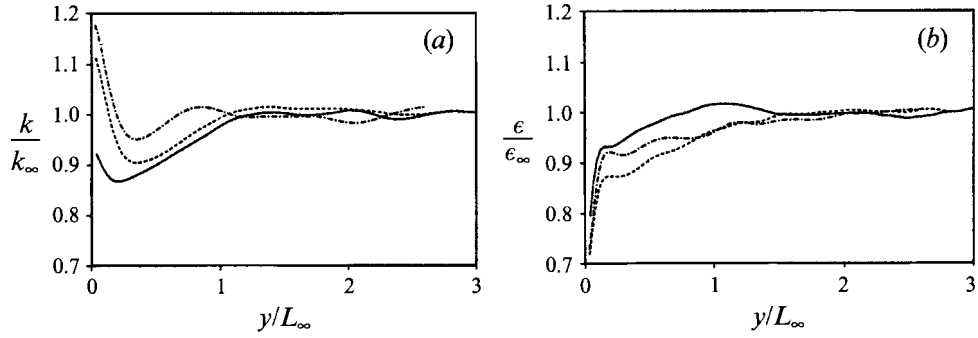


FIGURE 11. (*a*) Scaled turbulent kinetic energy, (*b*) scaled dissipation ($Re_T = 54$): ——, $t/T_0 = 0.1$; – – –, $t/T_0 = 1.1$; — · —, $t/T_0 = 2.1$.

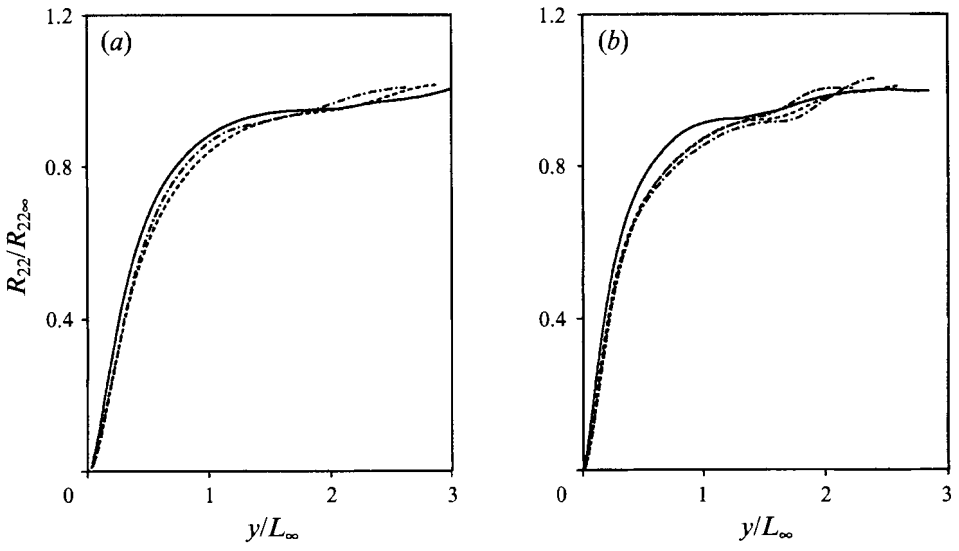


FIGURE 12. Scaled normal Reynolds stress profiles near an ideal free surface. (*a*) $Re_T = 54$, (*b*) $Re_T = 134$: ——, $t/T_0 = 0.1$; – – –, $t/T_0 = 1.1$; — · —, $t/T_0 = 2.1$; ———, $t/T_0 = 3.1$.

It is the imbalance between these two events which results in intercomponent energy transfer. Even more importantly, we will demonstrate in the next section that this imbalance between events is controlled by viscosity. Viscous effects are relatively small near a free surface, and therefore there is relatively little energy transfer.

Assuming that the previous explanation is valid, we then need to explain why the peak in the tangential Reynolds stress increases as time progresses. This increasing peak in the tangential stress has long been attributed to energy transfer and the splat event. The argument has been that since there is no turbulence production in this flow, any increase in the energy of one velocity component must be at the expense of the other turbulence component, and therefore the increase in the tangential stress near the wall must be a result of energy transfer from the normal component, with splats being the logical explanation for this transfer.

Although the previous argument is very convincing, we suggest another scenario: the increase in the tangential turbulent intensity with time is due to the normalization of the tangential intensity by its free-stream value. Essentially we are suggesting that the turbulence far from the wall decays faster than the turbulence near the wall, and the

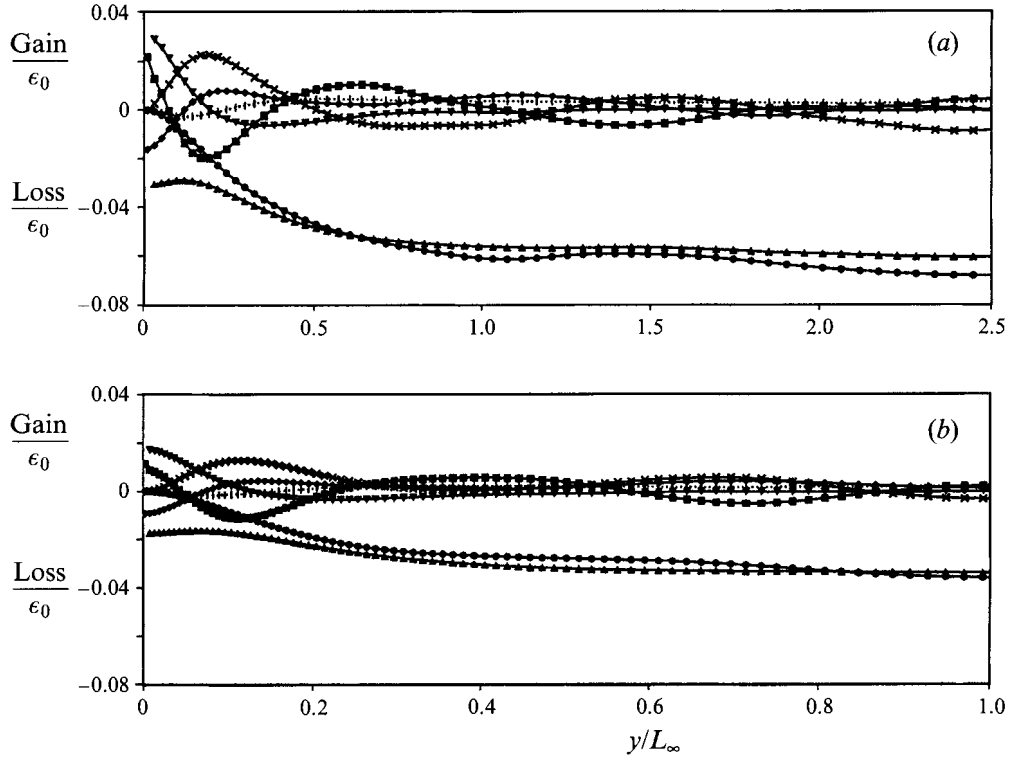


FIGURE 13. Terms in the normal Reynolds stress budget for turbulence near an ideal free surface ($t/T_0 = 3.0$). (*a*) $Re_T = 54$, (*b*) $Re_T = 134$. See figure 3 for legend.

phenomenon has nothing to do with energy transfer. To demonstrate this point, figure 11(*a*) shows the turbulent kinetic energy near a free surface. The turbulent kinetic energy shows a very similar behaviour to the tangential Reynolds stress. It has a peak near the boundary, which increases with time. There is no intercomponent energy transfer in the turbulent kinetic energy equation. Figure 11(*b*) confirms our suspicion that dissipation (not energy transfer) is responsible for this phenomenon. The figure shows that the dissipation does indeed decrease significantly near the surface. It is our conjecture that the two-componentality of the turbulence near the surface (and therefore the lack of the usual energy cascade) is responsible for this change in the dissipation rate near the surface.

The normal Reynolds stress near a free surface is shown in figure 12, for two Reynolds numbers and several different times. When the distance from the wall is normalized by the large-eddy lengthscale the curves quickly collapse to a single profile. The profiles at the earlist time (solid lines) are equivalent to the inviscid RDT analysis of Hunt & Graham. The later time profiles are in reasonable agreement with the RDT analysis, but the agreement appears to deteriorate somewhat as the Reynolds number increases.

The fact that the Hunt & Graham analysis applies to the boundary insertion problem and not to the subsequent evolution of turbulence near a boundary was recognized in a paper by Hunt (1984*a*). It has been suggested by Hunt (private communication) that the theory may still be applicable at long times because the timescales on which smaller eddies 'see' the boundary are relatively fast (since small eddies are swept towards the boundary by larger eddies). So in the frame of reference

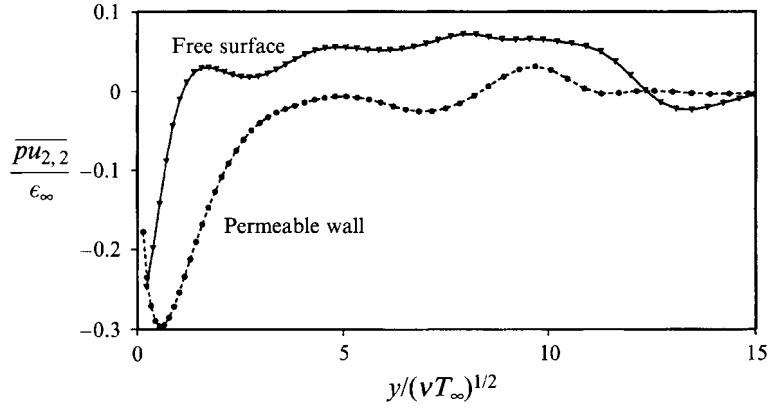


FIGURE 14. Pressure–strain term near a free surface and pressure–strain term near a permeable wall ($t/T_0 = 2.1, Re_T = 54$).

of small eddies, the boundary appears very suddenly, and the presence of the boundary is felt almost instantaneously. In Hunt (1984*b*) it was suggested that the theory is still valid as long as the dissipation does not vary significantly across the boundary layer.

The terms in the Reynolds stress evolution equation for the normal stress are shown in figure 13. Diffusion, dissipation, and turbulent transport are again the dominant terms. Pressure–strain and pressure transport are very significant but lesser contributors. Note that the pressure–strain term goes to zero (or positive) quite quickly. It is the dissipation and transport terms which are responsible for the scaling of the normal stress on $L_\infty$. The RDT analysis would suggest quite the opposite. Furthermore, since an inviscid RDT analysis is equivalent to neglecting the dissipation, diffusion, and turbulent transport terms, any agreement of the collapsed profiles in figure 12 with the RDT analysis is due to the cancellation of the dissipation, diffusion, and turbulent transport terms. No reason is apparent as to why this should occur. It is our conjecture that the processes at work near the free surface have relatively little to do with energy transfer (or the RDT analysis) except for the fact that the initial condition is given by that analysis.

A comparison of the pressure–strain term for the permeable wall and the ideal free surface at identical times and Reynolds numbers is shown in figure 14. The amount of energy transfer occurring near the permeable wall is significantly greater than that occurring next to the free surface. Again, this does not agree with what RDT would predict. A physical model which does explain this behaviour was discussed in reference to figure 8, and is explained further in the discussion. In terms of boundary conditions it implies that the condition on the normal velocity (i.e. wall blocking) is not the important condition to predict intercomponent energy transfer in the near-wall region. It is the condition on the tangential velocity (which was much stronger for the case of the permeable wall) which ultimately leads to energy transfer. Although subtle, this point of view is a considerable departure from past notions of how boundaries influence turbulence.

## 5. Solid wall

The presence of splats near a free surface was confirmed in §4. Whether these splats continue to be present near a solid wall and whether they are affected by the strong viscous effects near the wall is addressed in this next series of simulations (shear-

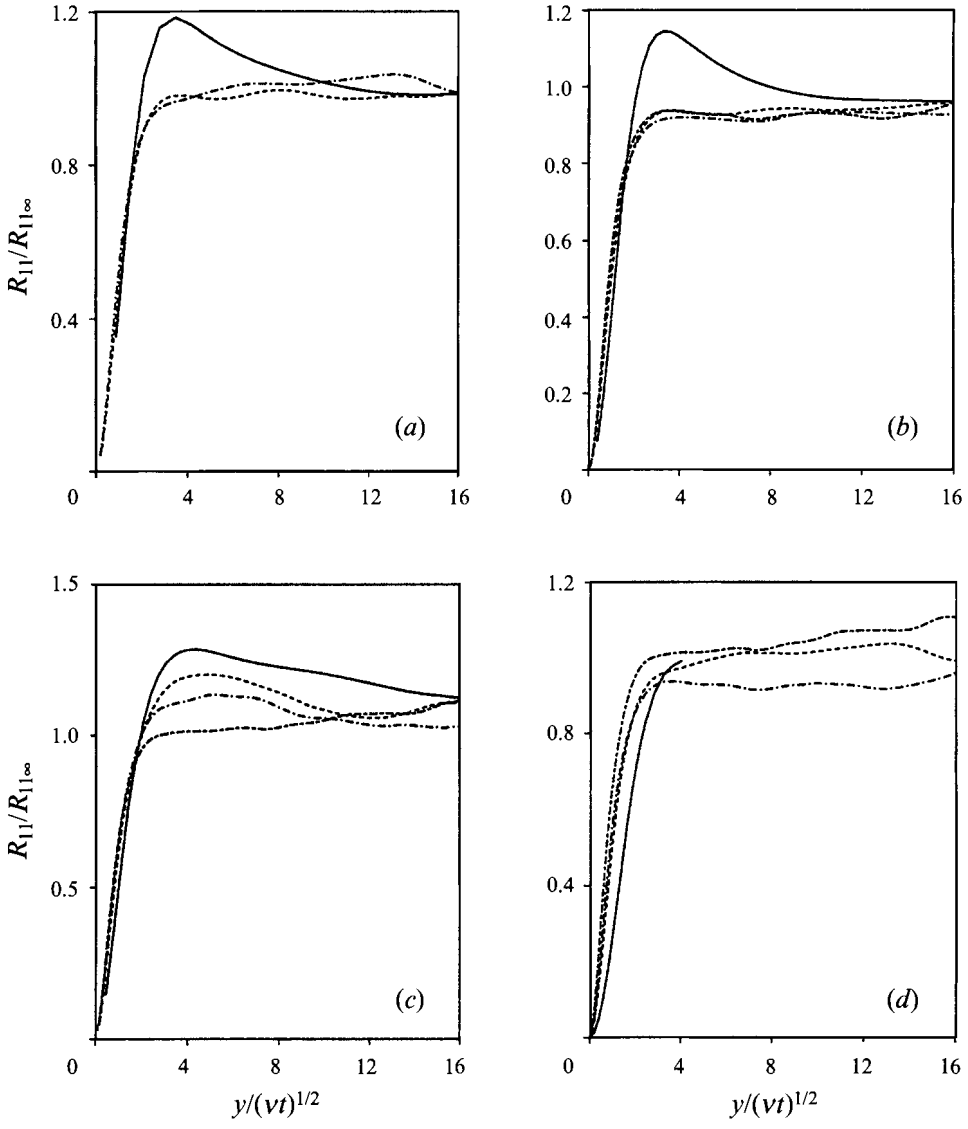


FIGURE 15. Tangential Reynolds stress profiles near a stationary solid wall: (*a*) $Re_T = 54$, (*b*) $Re_T = 134$, (*c*) $Re_T = 374$, (*d*) $t/T_0 = 3.1$. (*a–c*) See figure 12 for legend for $t/T_0$. (*d*) ——, $Re = 0$; – – –, $Re = 54$; — · —, $Re = 134$; — — —, $Re = 374$.

free turbulence near a solid wall). Instantaneous visualizations (similar to figure 8) are qualitatively identical to the free-surface results presented in figure 8 (when the same initial condition and Reynolds number are used). This suggests that splats (and antisplats) exist near the solid wall, even at relatively low Reynolds numbers ($Re_T = 54$), and that the structures near a shear-free wall do not change appreciably due to the effects of viscosity.

However, there are very significant differences between the two flows which cannot be identified by visual inspection. These differences are the result of viscosity. Although viscosity does not alter the basic form of near-wall structures (as implied in previous notions of the near-wall physics), it does alter the balance between splats and

antisplats. The small imbalance between splats and antisplats in the solid wall case leads to significant energy transfer.

The tangential Reynolds stress at $Re_T = 54$ is shown in figure 15(*a*). The peak near the wall at early times is a residual effect of the inhomogeneous initial condition at the time of wall insertion (see Appendix A). This initial peak in the tangential Reynolds stress is quickly dissipated by the viscous damping near the wall and, as in the permeable wall case, the profiles soon collapse to a single profile when scaled appropriately. Figures 15(*b*) and 15(*c*) show similar plots at Reynolds numbers 134 and 374 respectively. The higher Reynolds number case suffers from a poor statistical sample (only two realizations). We will focus only on the very near-wall results of the $Re_T = 374$ simulation (which appear to be statistically converged).

The Reynolds number dependence of the tangential Reynolds stress is summarized in figure 15(*d*). This figure shows the Reynolds stress profiles for four different Reynolds numbers at time $t/T_0 = 3.1$ (well after any residual effects due to the initial condition have subsided). The curve labelled $Re_T = 0$ is the same as that discussed in §3 (permeable wall) and used in figure 2. The lower Reynolds number cases agree qualitatively with the results of Uzkan & Reynolds.

Note that, as the Reynolds number increases, the profiles become steeper at the wall but do not penetrate farther into the flow. This suggests that there is a different mechanism at work here than in the permeable wall simulations (where turbulent transport was responsible for Reynolds number variations). Also note that the high Reynolds number simulation shows no peak in the tangential Reynolds stress near the wall at later times. This is contrary to the high Reynolds number experimental results of Thomas & Hancock, which showed an increase in the relative peak height as time progressed. The simplest explanation for this discrepancy is that the Reynolds number is still too low in these simulations. However, it is our conjecture that the tangential stress near a shear-free solid wall will never show a peak at long times, no matter how high the Reynolds number.

We suspect that the streamwise tangential intensities measured in the Thomas & Hancock experiment were contaminated by mean shear, despite the fact that they expended considerable effort trying to eliminate the effects of mean shear. Preliminary studies (by the present authors) of a shear-free channel flow (where the upper channel wall 'floated') showed that extremely small mean gradients could produce a production term which was comparable to the other terms in the Reynolds stress equations. In addition, preliminary studies (again by the present authors) of a spatially developing shear-free boundary layer (essentially identical to the experiments) showed that the streamwise derivatives present at the leading edge of the boundary layer were very large, and resulted in a non-uniform mean velocity profile near the wall (though no shear at the wall itself). The fact that the spanwise intensities measured in the Thomas & Hancock experiments do not show any peak near the wall (and were very unlikely to have been contaminated by production) confirms this hypothesis. Further evidence for the conjecture that no peak will occur at high Reynolds numbers is detailed below.

The terms in the tangential Reynolds stress evolution equation are shown in figure 16 for three different Reynolds numbers. As might be expected for a flow with strict boundary conditions on the tangential velocity, the dissipation and diffusion terms are large near the boundary. As the Reynolds number increases, the magnitudes of these terms increase somewhat, but their extent in viscous units, $(\nu t)^{1/2}$, remains almost unchanged.

The other term of importance in the balance is the pressure–strain term. The relative importance of the pressure–strain increases as the Reynolds number increases. At

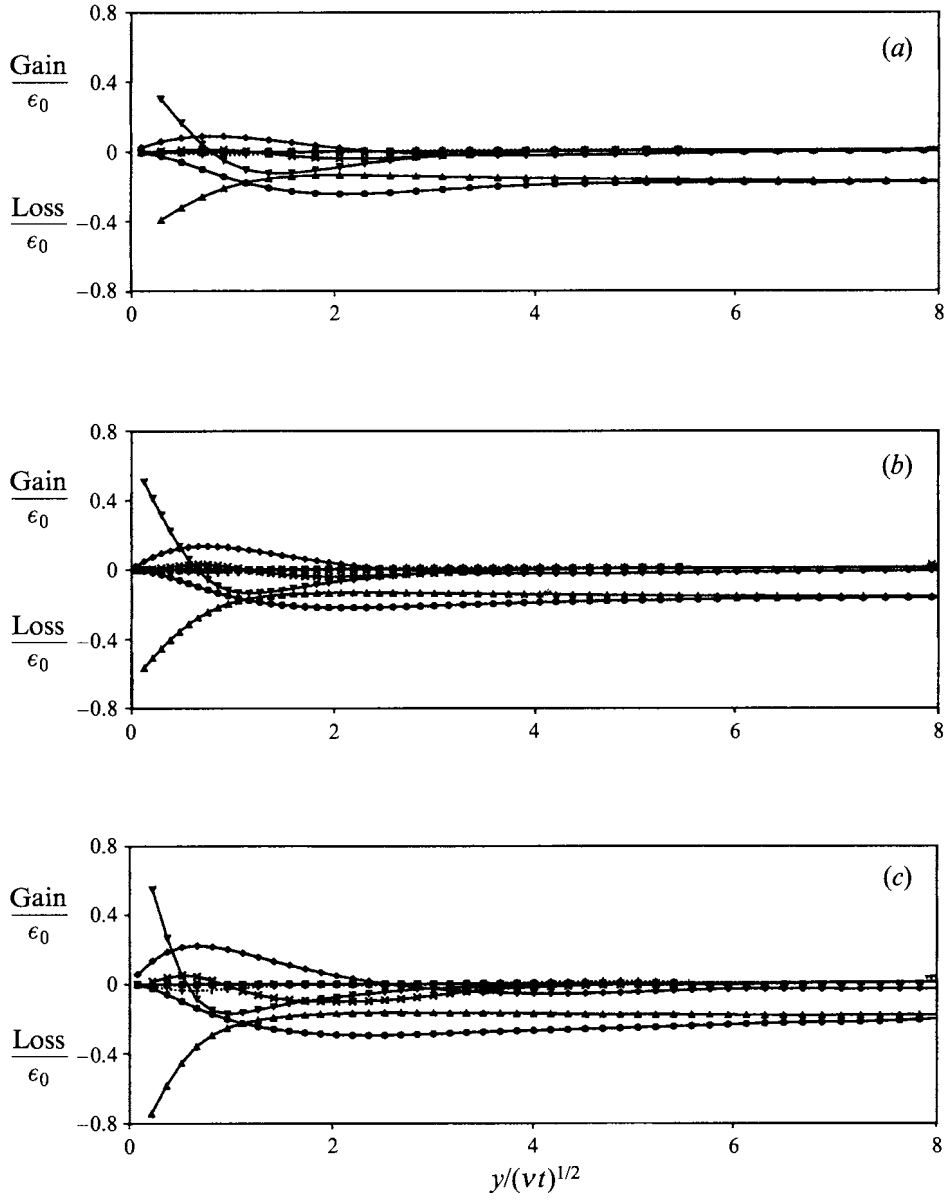


FIGURE 16. Terms in the tangential Reynolds stress budget for turbulence near a stationary solid wall ($t/T_0 = 1.0$). (*a*) $Re_T = 54$, (*b*) $Re_T = 134$, (*c*) $Re_T = 374$. See figure 3 for legend.

$Re_T = 374$ it makes a substantial contribution to the overall balance. Note that, as the Reynolds number increases, the extent of the pressure–strain term does not change significantly. This is consistent with the earlier conclusion that the extent of the pressure–strain term scales with $(\nu T_\infty)^{1/2}$ (since at long times $(\nu T_\infty)^{1/2} \approx (\nu t)^{1/2}$).

Interestingly, the turbulent transport is relatively small in this flow. The strong damping of the normal turbulence intensity inhibits the transport of turbulence by itself. This contrasts strongly with the case of the permeable wall, where turbulent transport was a significant term, and the contributions from pressure–strain were relatively minor. These differing mechanisms (energy transport versus intercomponent

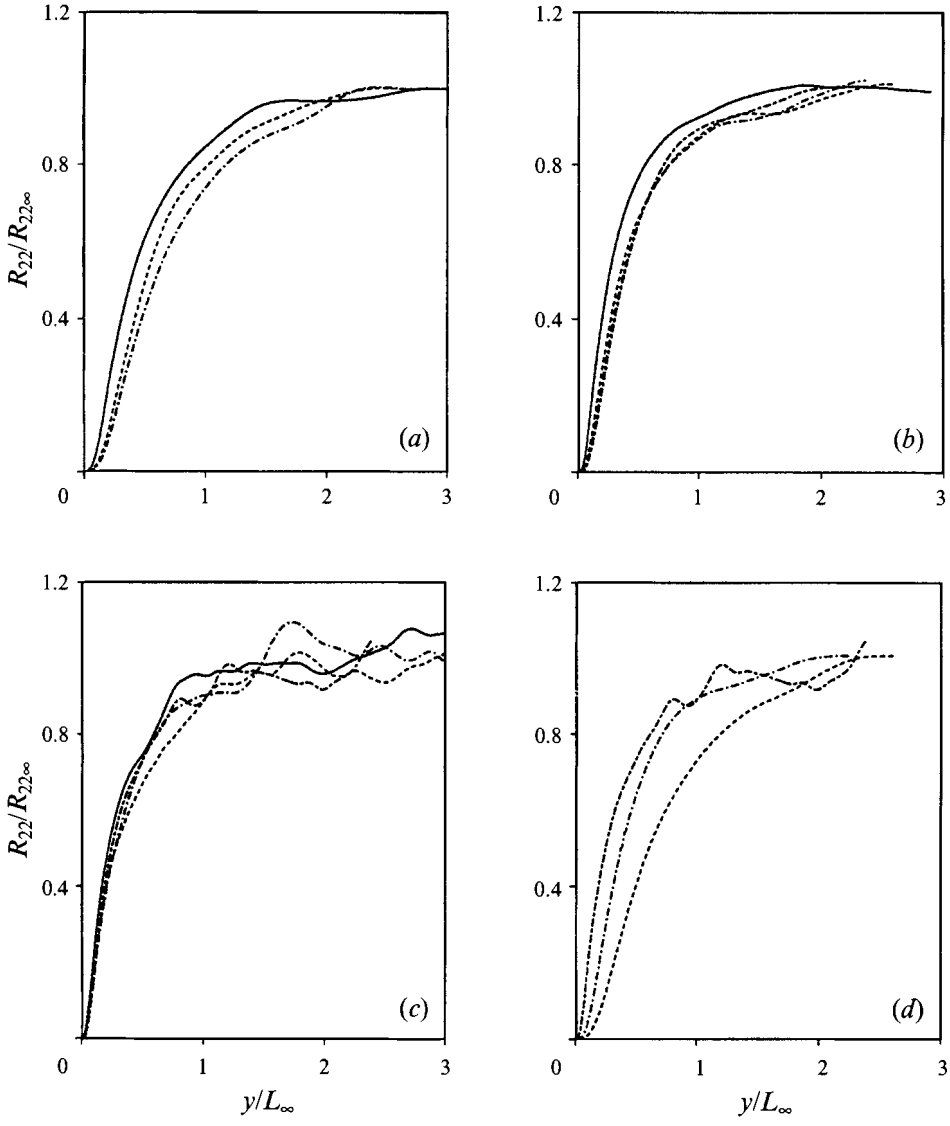


FIGURE 17. Normal Reynolds stress profiles near a stationary solid wall. (*a*) $Re_T = 54$, (*b*) $Re_T = 134$, (*c*) $Re_T = 374$, (*d*) $t/T_0 = 3.1$. (*a–c*) See figure 15 for legend.

energy transfer) explain why the Reynolds number variation of the tangential Reynolds stresses is different in the two flows. In the permeable wall case (with energy transport) the tangential Reynolds stress gradient becomes steeper near the wall at the expense of a reduced stress farther away from the wall. In the case of a solid wall (with intercomponent energy transfer) only a steepening of the profiles near the wall occurs.

The behaviour of the pressure–strain term suggests that at very high Reynolds numbers sufficient intercomponent energy transfer could occur to cause a peak in the tangential Reynolds stress. Although this is possible, we believe that it is unlikely. We have found that viscosity (specifically the amount of dissipation and diffusion near the wall) controls intercomponent energy transfer. Viscous damping removes energy close to the wall, which reduces the tangential energy available to drive the antisplat events. The end result is an imbalance between splats and antisplats and a net energy transfer.

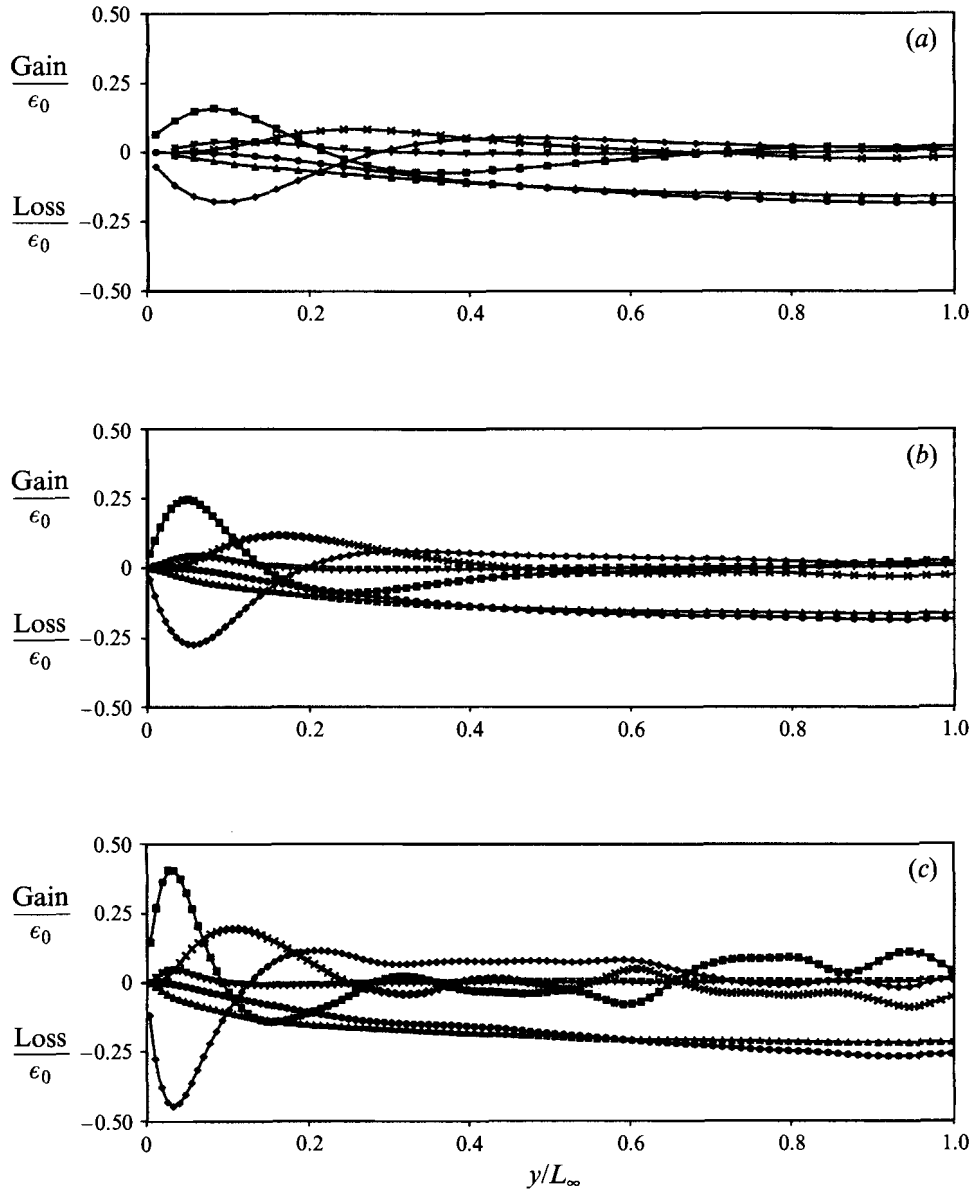


FIGURE 18. Terms in the normal Reynolds stress budget for turbulence near a stationary solid wall ($t/T_0 = 1.0$). (*a*) $Re_T = 54$, (*b*) $Re_T = 134$, (*c*) $Re_T = 374$. See figure 3 for legend.

Since dissipation and diffusion drive near-wall intercomponent energy transfer, it is unlikely that the pressure–strain term (representing energy transfer) will be larger than the dissipation and diffusion terms themselves (since this would result in feedback with an exponential growth). The fact that the pressure–strain and viscous terms act in the same region of the flow, $(\nu t)^{1/2}$, at long times implies that no peak is possible. Viscous damping is uniformly larger than intercomponent energy transfer in the region where the two processes are primarily active.

The normal Reynolds stress for the $Re_T = 54$ case is shown in figure 17(*a*). These profiles have a very similar shape to those found in the free-surface case. However, the

limiting behaviour near the wall is $O(y^4)$ in this case, instead of the $O(y^2)$ behaviour that is found near a free surface. Figures 17(*b*) and 17(*c*) show the normal Reynolds stress at Reynolds numbers of 134 and 374, respectively. The highest Reynolds number case, $Re_T = 374$, shows a great deal of noise in the far field due to an inadequate statistical sample, but gives reasonably good information close to the wall. The profile at $t/T_0 = 0.1$ is a good approximation to the inviscid Hunt & Graham solution. At later times the normal Reynolds stress appears to be approaching an 'equilibrium' solution which is slightly below the Hunt & Graham solution. This is very similar to the behaviour of the normal Reynolds stress near a free surface. The behaviour of the solution at long times, as a function of the Reynolds number, can be seen in figure 17(*d*). This plot shows that as the Reynolds number increases the normal Reynolds stress profile becomes fuller.

Despite the overall similarity of the normal Reynolds stress with the free-surface case, the underlying terms in the evolution equation are considerably different. Figure 18 shows budgets of the terms in the normal Reynolds stress equation. The dissipation and diffusion terms are relatively small. Pressure–strain and pressure transport dominate the near-wall balance. However, the two pressure terms balance very close to the wall, with pressure transport making up for any loss in energy due to the pressure–strain term. Slightly away from the wall, the turbulent transport term becomes important. As the Reynolds number increases, the magnitudes of the pressure terms and turbulent transport term increase.

Note that the pressure–strain term changes sign. It is negative very close to the wall (transferring energy to the tangential Reynolds stresses) but positive farther away from the wall. This behaviour is also seen in shearing wall-bounded flows such as turbulent channel flow. The behaviour farther away from the wall is thought to be due to standard return-to-isotropy mechanisms. A pressure–strain model based on this basic principle (and the idea that very near-wall pressure–strain is controlled by viscous processes) is developed in Part 2, and shows good agreement with the DNS data.

Although considerable emphasis has been placed on the importance of inter-component energy transfer in explaining near-wall physics, it is important to notice how significant energy transport is in the overall balance. Both the turbulent transport and pressure transport terms make relatively large contributions in this flow. These are terms which are often neglected or combined with other terms, but which contribute significantly in shear-free near-wall flows.

## 6. Discussion

We have suggested in the previous sections how the concepts of splats and antisplats can be used to explain the behaviour of turbulence near free surfaces and solid walls. We would now like to generalize those ideas to include the permeable wall, so that our conceptual model of the near-wall region is more universal and applicable to any type of boundary.

In the spirit of Prandtl (1925) we will discuss the interaction of blobs of fluid with the boundary. A blob, or region of fluid, moving towards the boundary is an impingement event, or a splat. Similarly, a blob of fluid moving away from the boundary is an ejection event, or antisplat. Splats transfer energy from the normal velocity component to the tangential velocity components. If there is little or no energy loss near the boundary (because of viscous effects), then the fluid will travel along the boundary until it encounters an antisplat, where the tangential energy will duly be

transferred back into normal energy. This is the situation near a free surface. However, if there are large viscous losses occurring near the boundary (such as in the solid wall case) then the tangential energy that is input to the antisplat events is only a fraction of that output by the splat events. This causes the antisplats to be slightly weaker than the splats on average, resulting in a net energy transfer from the normal velocity component to the tangential component.

In the case of the permeable wall, we still have splat and antisplat events as described in the generalized sense above. However, these structures are no longer stagnation-point regions but blobs of fluid which are about to pass through the permeable wall (splats) or which have just emerged from the permeable wall (antisplats). As in the solid wall case, there is an imbalance between these two events which is controlled by the viscous processes occurring very near the wall. This is explained as follows. Because of the $\partial v/\partial y = 0$ condition at the permeable wall, a blob of fluid does not pass through the wall unaltered. A region of high pressure develops on the wall which distorts the blob (squashes it) until the condition is satisfied. As the blob exits the wall the process reverses, with the blob of fluid unsquashing back to its normal shape. However, in going from the unsquashed to the squashed state, energy is transferred from the normal velocity to the tangential velocity. If this tangential energy is quickly dissipated (as it is near the permeable wall) then as the blob emerges from the permeable wall, it has less energy. So owing to viscous effects near the permeable wall, antisplats are less energetic than splats, and there is a net intercomponent energy transfer.

It is clear that in terms of intercomponent energy transfer, the solid wall has more in common with the permeable wall than it does with the free surface. Despite the similarities in the structures of the free surface and solid wall, and despite the presence of wall blocking in both cases, those two boundaries have very different intercomponent energy transfer effects. It is not the boundary conditions on the normal velocity which effect energy transfer, but the boundary conditions on the tangential velocity. Furthermore, viscosity (and energy removal) controls intercomponent energy transfer near boundaries. These surprising conclusions are reinforced by the fact that the pressure–strain term scales on the length $(\nu T_\infty)^{1/2}$, and not on the integral length-scale $L_\infty$.

The term splat was originally used in the context of turbulence energetics and modelling close to a wall. It was an attempt to describe the consequences of flow impingement near a solid boundary. Numerous ejection and impingement type events have been described in the context of turbulent boundary layers in the literature. For example, it is well known (Falco 1988, 1991; Jimenez & Moin 1991; Orlandi & Verzicco 1993) that when a vortical structure is close to a solid wall it produces vorticity of the opposite sign at the wall, which can then be ejected away by the primary vortex. Such an ejection scenario does involve splats and antisplats, but it also involves more complicated dynamics than is envisioned in the present study. Here, the splats and antisplats are simple consequences of the equation of continuity (not coherent vortical structures) near any type of boundary (not just solid walls).

In summary, these simulations have confirmed that splats do exist, even at very low Reynolds numbers. However, splats are not responsible for intercomponent energy transfer near boundaries, since in the free-surface case there were splats but little intercomponent energy transfer. Furthermore, intercomponent energy transfer does not cause an increase in the tangential turbulent intensity near the boundary (a peak). In the free surface case where a peak was present, it was due the normalization by the free-stream value, and reduced dissipation near the boundary. In the solid wall case, no peak was observed, although intercomponent energy transfer was very significant.

Intercomponent energy transfer near boundaries is due to splat events and antisplat events and, in particular, the imbalance between these events. The imbalance between splats and antisplats is thought to be controlled by viscous processes near the wall. For this reason, boundaries with strict conditions on the tangential velocity (solid wall and permeable wall) have larger intercomponent energy transfer effects than those with a looser condition (free surface).

Although we have emphasized the causes and effects of intercomponent energy transfer near boundaries in this work, we note that the Reynolds stress equation budgets show that all the terms in the equation (not just the pressure–strain) are significant. Although conceptually these are very simple flows, in practice the inhomogeneity and anisotropy generated by the boundary makes them challenging to model accurately. We present some of our ideas on modelling near-wall flows in Part 2.

Financial support for this work was provided by the National Science Foundation, and the Center for Turbulence Research. Supercomputer time on the Connection Machine was provided by the NAS division of NASA-Ames Research Center. The authors would like to thank Peter Bradshaw for his many useful comments during the course of this work.

## Appendix A. The inviscid Hunt & Graham analysis

The Hunt & Graham analysis is based on rapid distortion theory (RDT), where the Navier–Stokes equations are linearized and the products of fluctuating velocities (found in the convective term) are neglected. The inviscid analysis further assumes that at high enough Reynolds numbers viscous effects can be neglected. This section provides an alternative derivation of the classic Hunt & Graham analysis, which may help to clarify some of its limitations.

For temporally developing turbulence with no mean velocity (such as the flows considered in this work) the inviscid RDT equations are

$$\boldsymbol{u}_{i,t} = -p_{,i}, \quad \boldsymbol{u}_{i,i} = 0, \tag{A 1a, b}$$

where $\boldsymbol{u}$ is the fluctuating velocity, and $p$ is the pressure. The equivalent system of equations can be found in the original Hunt & Graham (1978) paper, with the slight difference that the Hunt & Graham equations are for uniformly convected turbulence (the spatially developing boundary layer), whereas the temporally developing boundary layer is being considered here. Ultimately the Hunt & Graham system is solved in a uniformly convecting frame of reference (change of variables) so the two equation systems are identical.

Equation (A 1*a*) is linear and can be solved, given an initial spectrum, in spectral space. This is the approach taken in the original paper, with the ultimate result being an equation which expresses the final spectrum in terms of an initial spectrum. Energy spectra and r.m.s. intensities are then predicted for the cases of an initial von Kármán spectrum and an initial Townsend spectrum. These initial energy spectra result in a decrease (to zero) of the normal turbulent intensity as the boundary is approached. The energy lost by the normal intensity is transferred to the two tangential intensity components, so they show an increase as the boundary is approached. The influence of the boundary on the turbulence components exists over a distance of roughly one large-eddy length.

The view taken here is significantly different from that of Hunt & Graham. Note that (A 1 *a*) represents a projection of an initially divergent vector field into the space of divergence-free vector functions. Integrating (A 1 *a*) over the time interval $t^-$ to $t^+$ gives

$$u_i|_{t^+} - u_i|_{t^-} = -\tilde{p}_{,i}, \tag{A 2}$$

where $\tilde{p}$ is the integral of the pressure over the time interval. Using the continuity equation it is clear that if both the initial ($t^-$) and the final ($t^+$) velocity fields are divergence free, then the equation for the pressure is $\tilde{p}_{,ii} = 0$. With Neuman boundary conditions this equation has the trivial solution $\tilde{p}$ is a constant. Therefore, the final and initial velocity fields are identical. In short, only if the initial field is divergent will any change in the velocity field occur. Then the integrated pressure is a solution of $\tilde{p}_{,ii} = u_{i,i}|_{t^-}$ with Neumann boundary conditions, and the final velocity field can be found from (A 2).

The crucial observation here is that divergent velocity fields occur only very rarely. A key instance is when a wall or surface (with $v = 0$) is suddenly inserted into a turbulent flow. The only variable which can respond in such a short time frame is the pressure, which owing to its elliptic nature can respond instantaneously. If the full Navier–Stokes equations are integrated in time, and the time interval is prescribed to begin just before and to end just after the boundary insertion, then (A 2) will again be recovered. The convective and diffusive terms integrated over an extremely small interval will be negligible. Only the pressure term, which is essentially a delta function, will remain finite.

Three major conclusions can be drawn from this analysis. First, the Hunt & Graham analysis actually applies to the boundary insertion problem (or leading-edge problem for the spatially developing case). It is, in fact, an exact analysis for the case of boundary insertion.

The second conclusion is a corollary to the first. The Hunt & Graham analysis does not apply to the subsequent evolution of turbulence near boundaries. After boundary insertion, the velocity field is divergence free and remains so. The subsequent evolution depends on dynamics, specifically the convective and diffusive terms that are neglected in the analysis. It is noteworthy that despite this result there is considerable evidence supporting the application of RDT analysis at long times (see Hunt 1984*a*).

The final conclusion is of a practical nature. Boundary insertion can be simulated using a Navier–Stokes code (reproducing the Hunt & Graham theoretical results) by drastically reducing the computational time step when the boundary is inserted. This effectively causes the convective and diffusve terms to become extremely small, and allows the pressure to appropriately project the velocity field into the function space of divergence-free vector fields.

## Appendix B. The viscous Hunt & Graham analysis

The Hunt & Graham paper also proposed solutions for the very near-wall region of wall-bounded turbulent flows, where viscous effects dominate. The initial starting point was again rapid distortion theory but this time, rather than neglecting the diffusion terms (inviscid analysis), the pressure terms were assumed to be small. The resulting equations for the velocity components in temporally developing turbulence are then

$$u_{i,t} = (1/Re)\, u_{i,kk}. \tag{B 1}$$

This has the form of a heat equation, with an error-function solution (equation (2.26) in the original paper).

This error-function solution was plotted along with simulation results in their figure 3, and has the label '$Re_T = 0$'. It has this title because as the turbulent Reynolds number decreases the turbulent transport terms and the pressure–strain term become less important in the Reynolds stress budget. Equation (B 1) effectively neglects these terms in the budget, and hence corresponds to the $Re_T = 0$ limit. Note (figure 2) that even at very low Reynolds numbers, (B 1) is not a very good approximation.

## REFERENCES


BATCHELOR, G. K. 1956 *The Theory of Homogeneous Turbulence*, p. 47. Cambridge University Press.

BIRINGEN, S. & REYNOLDS, W. C. 1981 Large-eddy simulation of the shear-free turbulent boundary layer. *J. Fluid Mech.* **103**, 53–63.

BRADSHAW, P. & BOTT, D. M. 1993 A moving-floor test section for simulating high free-stream turbulence. *AFOSR Contractors Meeting – August 1993*, p. 4.1–1.

BRUMLEY, B. 1984 Turbulence measurements near the free surface in stirred grid experiments. In *Gas Transfer at Water Surfaces* (ed. W. Brutsaert & G. H. Jirka), pp. 83–92. Reidel.

DURBIN, P. A. 1993 A Reynolds stress model for near-wall turbulence. *J. Fluid Mech.* **249**, 465–498.

FALCO, R. E. 1988 Vortex ring/viscous wall layer interaction model of the turbulence production process near walls. *Exps. Fluids* **6**, 305–315.

FALCO, R. E. 1991 A coherent structure model of the turbulent boundary layer and its ability to predict Reynolds number dependence. *Phil. Trans. R. Soc. Lond.* A **336**, 103–129.

HALLBACK, M. & JOHANSSON, A. V. 1992 Modeling of pressure-strain in homogeneous turbulence. *Advances in Turbulence 4* (ed. F. T. M. Nieuwstadt). Springer.

HARLOW, F. H. & WELCH, J. E. 1965 Numerical calculation of time-dependent viscous incompressible flow of fluid with free surface. *Phys. Fluids* **8**, 2182–2189.

HUNT, J. C. R. 1984*a* Turbulence structure and turbulent diffusion near gas–liquid interfaces. In *Gas Transfer at Water Surfaces* (ed. W. Brutsaert & G. H. Jirka), pp. 67–82. Reidel.

HUNT, J. C. R. 1984*b* Turbulence structure in thermal convection and shear-free boundary layers. *J. Fluid Mech.* **138**, 161–184.

HUNT, J. C. R. & GRAHAM, J. M. R. 1978 Free-stream turbulence near plane boundaries. *J. Fluid Mech.* **84**, 209–235.

JIMENEZ, J. & MOIN, P. 1991 The minimal flow unit in near wall turbulence. *J. Fluid Mech.* **225**, 213.

KIM, J. & MOIN, P. 1985 Application of a fractional-step method to incompressible Navier–Stokes equations. *J. Comput. Phys.* **59**, 308–323.

KLINE, S. J., REYNOLDS, W. C, SCHRAUB, F. A. & RUNSTADLER, P. W. 1967 The structure of turbulent boundary layers. *J. Fluid Mech.* **30**, 741–773.

LE, H. 1994 Direct numerical simulation of turbulent flow over a backward facing step. PhD thesis, Dept of Mech. Engng, Stanford University.

LEE, M. J., KIM, J. & MOIN, P. 1990 Structure of turbulence at high shear rate. *J. Fluuid Mech.* **216**, 561–583.

LILLY, D. K. 1965 *Mon. Weather Rev.* **93**, 11.

MADAY, Y., PATERA, A. T. & RONQUIST, E. M. 1990 An operator-integration-factor splitting method for time-dependent problems: application to incompressible fluid flow. *J. Sci. Comput.* **5**, 263–292.

MALAN, P. & JOHNSTON, J. P. 1993 Heat transfer in shear-free turbulent boundary layers. *Rep.* MD-64. Department of Mechanical Engineering, Stanford University.

MOIN, P. 1987 Analysis of turbulence data generated by numerical simulations. *AIAA 25th Aerospace Sciences Meeting, January 1987, Reno, Nevada. AIAA Paper* 87-0194.

ORLANDI, P. & VERZICCO, R. 1993 Vortex rings impinging on walls: axisymmetric and three-dimensional simulations. *J. Fluid Mech.* **256**, 615–646.

PEROT, J. B. 1992 Direct numerical simulation of turbulence on the Connection Machine. In *Parallel Computational Fluid Dynamics '92* (ed. R. Pelz, A. Ecer & J. Hauser), pp. 325–336. North-Holland.

PEROT, J. B. 1993 An analysis of the fractional step method. *J. Comput. Phys.* **108**, 51–58.

PEROT, J. B. & MOIN, P. 1993 Shear-free turbulent boundary layers. *Rep.* TF-60. Dept. of Mech. Engng, Stanford University.

PEROT, J. B. & MOIN, P. 1995 Shear-free turbulent boundary layers. Part 2. New concepts of Reynolds stress transport equation modelling of inhomogeneous flows. *J. Fluid Mech.* **295**, 229–245.

PRANDTL, L. 1925 Über die ausgebildete Turbulenz. *Z. Angew. Math. Mech.* **5**, 136.

REYNOLDS, W. C. 1991 The potential and limitations of direct and large eddy simulations. In *Whither Turbulence* (ed. J. L. Lumley). Lecture Notes in Physics, vol. 357, pp. 313–315. Springer.

ROBINSON, S. K. 1991 Coherent motions in the turbulent boundary layer. *Ann. Rev. Fluid Mech.* **23**, 601.

ROTTA, J. 1951 Statistical Theory of inhomogeneous turbulence. Part I. *Z. Phys.* **129**, 257–572.

THOMAS, N. H. & HANCOCK, P. E. 1977 Grid turbulence near a moving wall. *J. Fluid Mech.* **82**, 481–496.

UZKAN, T. & REYNOLDS, W. C. 1967 A shear-free turbulent boundary layer.*J. Fluid Mech.* **28**, 803–821.